Advanced techniques in GEO 600

2014 Class. Quantum Grav. 31 224002

(http://iopscience.iop.org/0264-9381/31/22/224002)

IOP Publishing Classical and Quantum Gravity
Class. Quantum Grav. 31 (2014) 224002 (26pp) doi:10.1088/0264-9381/31/22/224002

Advanced techniques in GEO 600

C Affeldt[1], K Danzmann[1], K L Dooley[1], H Grote[1], M Hewitson[1], S Hild[2], J Hough[2], J Leong[1], H Lück[1], M Prijatelj[3], S Rowan[2], A Rüdiger[1], R Schilling[1], R Schnabel[1], E Schreiber[1], B Sorazu[2], K A Strain[2], H Vahlbruch[1], B Willke[1], W Winkler[1] and H Wittel[1]

[1] Max-Planck-Institut für Gravitationsphysik (Albert-Einstein-Institut) und Leibniz Universität Hannover, Callinstr. 38, D-30167 Hannover, Germany
[2] SUPA, School of Physics and Astronomy, The University of Glasgow Glasgow G12 8QQ, UK
[3] European Gravitational Observatory (EGO), I-56021 Cascina (Pi), Italy

E-mail: hartmut.grote@aei.mpg.de

Received 11 July 2014, revised 7 September 2014
Accepted for publication 22 September 2014
Published 4 November 2014

Abstract

For almost 20 years, advanced techniques have been developed and tested at the GEO 600 laser-interferometric gravitational wave detector. Many of these innovations have improved the sensitivity of GEO 600 and could be shown to be consistent with stable and reliable operation of gravitational wave detectors. We review the performance of these techniques and show how they have influenced the upgrades of other detectors worldwide. In the second half of the paper, we consider how GEO 600 continues to pioneer new techniques for future gravitational wave detectors. We describe some of the new methods in detail and present new results on how they improve the sensitivity and/or the stability of GEO 600 and possibly of future detectors.

Keywords: gravitational wave detector, laser interferometer, advanced detector
PACS numbers: 04.80.Nn, 07.60.Ly, 95.55.Ym

(Some figures may appear in colour only in the online journal)

1. Introduction

GEO 600 [1, 2] is the British–German laser-interferometric gravitational wave detector (GWD), with 600 m long beam tubes, located 20 km south of Hannover in Germany. Construction of GEO 600 started in 1995, and the project progressed in sequential commissioning and data-taking phases, similar to the LIGO [3] detectors in the US, and the Virgo [4] detector

in Italy. These detectors, together with the TAMA 300 [5] detector in Japan, formed the *first generation* laser-interferometric GWD network. While LIGO and Virgo feature 4 km and 3 km long arms, respectively, in GEO 600 the aim was to partially compensate its shorter 600 m arm-length by employing *novel techniques*, not employed by LIGO, Virgo and TAMA. Even though some of them were untested and risky, the GEO 600 team was able to incorporate and commission all novel techniques to the benefit of the GEO 600 sensitivity and to the benefit of second-generation GWDs, such as advanced LIGO [6], advanced Virgo [7] and the new Japanese KAGRA [8] detector. In contrast to the LIGO and Virgo projects, which dismantled their initial detectors and installed and commissioned almost completely new designed detector subsystems in one step, the GEO 600 group decided to follow the path of sequential upgrades in the GEO-HF [9] program, which started in 2009. In this program, which targets mainly a sensitivity improvement at *high frequencies*, *advanced techniques* are used, some of which are again pioneered, as they are not installed in the second generation detectors of the LIGO, Virgo and KAGRA projects.

The outline of this paper is as follows: in section 2, we summarize a number of advanced techniques that were implemented in GEO 600 before the start of the GEO-HF program in 2009. From section 3 on, we discuss a selection of advanced techniques implemented since the start of the GEO-HF upgrade program. Section 3 covers the topic of active thermal compensation techniques, both implemented and planned, and discusses a new measurement of the thermal lens in the beam-splitter of GEO 600. Section 4 covers new results from squeezed-light application in GEO 600, including a new record squeezing level of 3.7 dB, and new results on the long-term performance of the squeezing application. We further give an overview of a new phase control scheme and of the first demonstration of an automatic alignment system for squeezing. Finally, section 5 introduces a new technique to derive signals for alignment control of the output mode-cleaner, a control task that has proven to be particularly demanding.

1.1. Detector overview

Figure 1 shows a simplified optical layout of GEO 600. A laser-diode-pumped solid state laser system generates 30 W of linear-polarized single-frequency radiation at 1064 nm [10]. This laser system inherits its superb frequency stability from the 2 W Nd:YAG non-planar ring oscillator which seeds four Nd:vanadate amplifier stages to increase the power. Identical laser systems have proven their reliability in the last two years of the first LIGO phase (eLIGO) and are used as master lasers to seed the advanced LIGO 200 W injection-locked laser system [11, 12].

The laser beam is injected into a sequence of two vacuum-suspended triangular input mode-cleaners which are used for spatial and temporal filtering of the laser beam. The mode-cleaner mirrors are suspended as double pendulums to decouple them from ground motion. For control purposes, a set of five phase modulations at radio frequencies f1–f5 is applied to the light via electro-optic modulators. The in-vacuum modulators for f2–f5 are made of rubidium–titanyle–phosphate.

After passing the mode-cleaners and modulators, the beam enters the main interferometer section, a dual-recycled Michelson interferometer [13, 14] with mirrors suspended as triple pendula (except MPR, which is supported by a double pendulum suspension). The transmissivity of the power recycling mirror MPR is $T = 0.09\%$, resulting in a power recycling factor of about 900 in the actual experiment, mainly limited by small-angle scatter losses of the main optics. The arms of the Michelson are folded once in the vertical plane, to yield an effective arm-length of 1200 m. The signal recycling (SR) mirror MSR has a transmissivity of

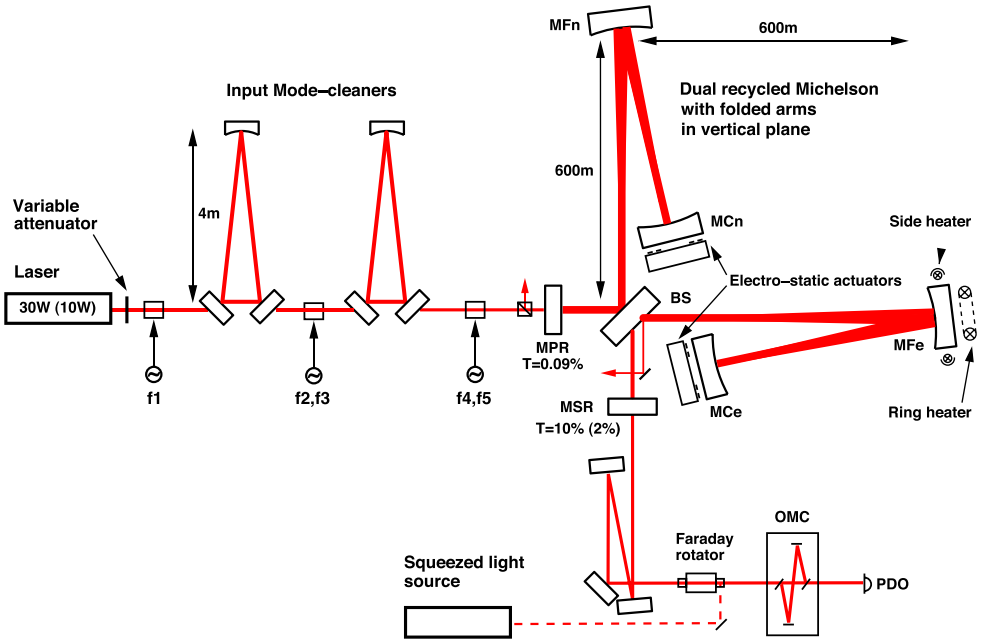

Figure 1. Simplified optical layout of the GEO 600 detector. GEO 600 is a dual (power- and signal-) recycled Michelson interferometer with single folded arms within 600 m long beam tubes. The squeezed light source, Faraday rotator and output mode cleaner (OMC) were added in 2009/2010 as part of the GEO-HF program. Numbers in brackets denote values before 2010. All components shown (except for the laser, attenuator and squeezed light source) are contained in a vacuum enclosure. See text for more details.

$T = 10\%$ ($T = 2\%$ before 2010). A small fraction of the injected light, which carries the GW information, leaves the dual recycled Michelson via a beam reduction telescope towards the detection photo-diode PDO. Until 2009, GEO 600 was running mainly in detuned SR [15] mode with heterodyne readout [2]. As part of the GEO-HF program, the output optic section was extended to include a Faraday rotator for squeezed-light injection, and an output mode-cleaner. After 2009, GEO 600 was running mainly in tuned SR mode with homodyne (*DC*) readout [16] and squeezed-light injection [17, 18].

2. Advanced techniques prior to the GEO-HF program

The techniques described in this section are the corrugated beam tube, triple pendulum suspensions, monolithic stage, electrostatic drives (ESDs), a ring heater, SR, and strain calibration. While other GW projects use a solid beam tube, the corrugated design might be interesting for future detectors to minimize cost. Multiple-stage suspensions have been used in Virgo from the beginning, however, the integrated design of multiple-stage suspensions with a monolithic last stage, electrostatic actuators and a reaction chain in GEO 600 has been the precursor for the very similar suspension design in advanced LIGO. SR has been used in GEO 600 instead of arm cavities as in LIGO, Virgo, and TAMA 300, but has been added to the advanced detector designs. And finally, the calibration technique used in GEO 600 explored the calibration of detuned SR and features quasi-real-time fitting of optical parameters.

2.1. Beam tube design

In order to extend GEO 600 from the initially planned length of 300–600 m, the costs for the beam tube had to be reduced to a minimum, while still ensuring durability and obtaining a low outgassing rate [19]. A low outgassing rate and corrosion resistance required the use of high quality stainless steel, hence AISI 316LN was chosen. The costs were reduced by using thin-walled tubes of only 0.9 mm wall thickness. This also reduced the weight, easing handling, and reducing the cost of suspending the tube. A thin-walled tube can withstand the outside air pressure only if it is enforced with many stiffening rings or if it is deeply corrugated to give sufficient radial stiffness. In the case of GEO 600, the shape of the corrugation is nearly semicircular with a corrugation period of 3 cm and a depth of 1.7 cm. The tube diameter is 0.6 m. No detrimental effect of the corrugation with respect to scattered light is expected, since baffles mounted at the proper distances within the tube, prevent any stray laser light from the end mirrors to hit any place of the steel wall.

The tube was fabricated by welding cylinders from sheet metal and corrugating it by first forming it in a hydraulic press and then rolling the final shape of the corrugations to a smooth shape, resulting in 75 cm sections of corrugated tube. Sets of six of these elements were TIG-welded together with an orbital welding machine and cleaned and leak-tested at the factory. These 4.5 m sections were doubly sealed in plastic bags, transported to the GEO 600 site and transferred into one of the GEO 600 end buildings. These provided a clean working environment where the sections were welded to the already finished part of the tube. In this process the whole tube, being suspended by kevlar rope slings, was rotated around its axis. As each section was joined the whole tube was pushed outwards by the length of one section. To allow this, the tube was suspended from small trolleys that could move along an aluminium rail mounted above the tube.

Leak testing of the tube, by wrapping 3 m sections with plastic sheets, injecting helium gas, and detecting leakage with a residual gas analyser at the ends of the tubes, revealed about ten leaks in total. Due to the prior leak testing of the 4.5 m section at the factory all leaks were located at welds done on site. Some of the leaks were welded *in situ* and others were closed by applying Ceramabond, a vacuum and high temperature compatible glue. Some minor leaks in the central cluster of vacuum tanks (not in the tube), which could not be found, are still present today and dominate the gas composition at a pressure level of 2×10^{-6} Pa. In the end stations the pressure is governed by hydrogen from the stainless steel of the tube and air from the central cluster at about 2×10^{-7} Pa.

Ultra-high vacuum compatibility requires removing all contaminants, e.g. water or hydrocarbons, from the tube walls and reducing outgassing to a minimum. Hydrogen dissolved in the metal is one of the major sources of residual gas in a stainless steel UHV system. An oxide layer on the stainless steel surface, produced by heating the tube in air to a few hundred centigrade, acts as a diffusion barrier reducing the hydrogen outgassing from the tube walls. The optimum thickness of this oxide layer is a matter of debate and several experiments performed by different groups yielded different results (see [20, 21] and references therein). The GEO 600 team decided to go for an average procedure, and baked the tube for two days at 200 °C, while flushing it with dried air. The tube was then evacuated and baked at 250 °C for five days. The tube was heated by applying a dc voltage of 300 V between the tube and the aluminium rail, now serving as a current return path, resulting in a current of 600 A. Thermal insulation was provided by a 20 cm layer of rock wool. Baking of the tube was completed in 1998. The vacuum tube has been stable for almost two decades of operation of GEO 600 without developing significant leaks. The pressures in the end stations suggest an upper limit of air leak-rate of 8×10^{-6} mbar $\ell\ s^{-1}$ for the whole 1200 m of beam tube. A test performed

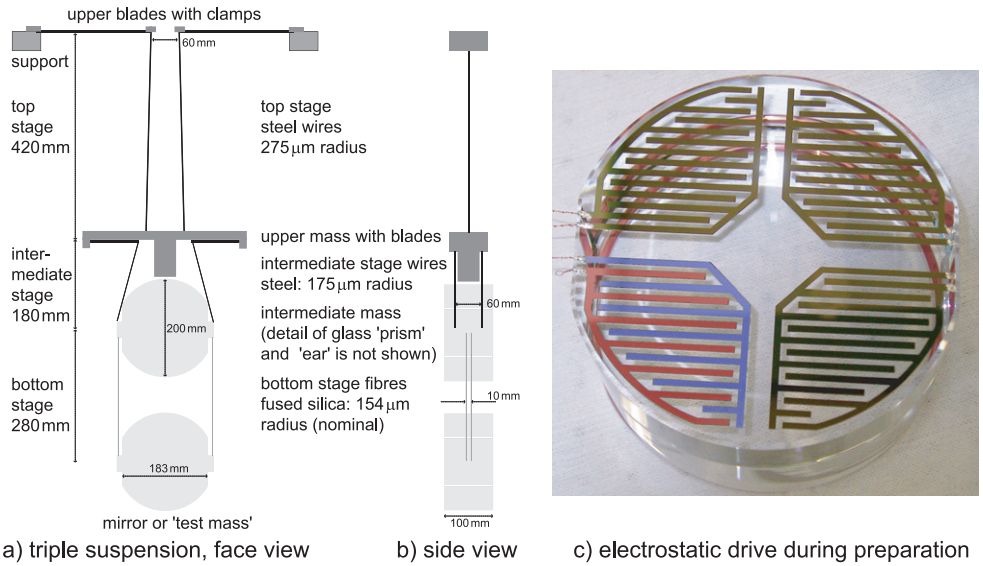

Figure 2. Panels (a) face view and (b) side view illustrate the triple suspension. Spring steel parts are shown in black, other metal parts are in mid-grey and fused-silica parts are in light grey. Detail of the various clamps and other attachments for wires and fused-silica fibres are not shown. Panel (c) shows a modified photograph of an electrostatic drive during final preparation for installation.

at Rutherford Appleton Labs in the UK with a 1.5 m diameter tube has shown that the technique is scalable to larger beam tubes, such that it can be considered a cost-effective alternative design for possible future detectors with very long arms.

2.2. Triple pendulums

In GEO 600, *triple pendulum suspensions*, i.e. assemblies consisting of three pendulums hung one-from-another in cascade, are employed to provide a low-dissipation support for the mirrors and to isolate them from external vibration. In this section we review the suspension design with respect to vibration isolation and control. In the next section we consider the design of the bottom stage to minimize thermal noise.

High-frequency vibrations are easier to isolate, so it is the low-frequency end of the observing band that creates the greatest challenge for isolation. In GEO 600 the relevant sensitivity goal is 7×10^{-20} m $\mathrm{Hz}^{-1/2}$ at 50 Hz. In the design of the suspension an upper limit for the contribution to this from residual seismic noise was set at 10% of that value. Sketches of the suspension are shown in panels (a) and (b) of figure 2. For further detail see [22].

Although the GW measurement is most sensitive to motion along the arms of the interferometer, off-axis vibration may cross-couple into the interferometric measurement along the longitudinal direction. The most serious cross-coupling, which may be as large as 10^{-3}, is from the vertical direction. Such coupling arises in all interferometric detectors due to the curvature of the Earth's surface and, possibly, imperfect levelling, but in GEO 600 there is also a contribution from the geometry of the arms which are folded in vertical planes.

Sufficient isolation in the longitudinal direction is easily achieved by cascading pendulums in series. Due to the stiffness of conventional suspensions, however, additional springs are needed for vertical isolation. The design of the bottom stage is constrained by the need for

low thermal noise, therefore vertically-compliant metal springs were incorporated only into the upper two stages of the triple pendulum design.

From top to bottom, the masses of the suspension chain hang on two wires, four wires and four silica fibres, respectively. The top mass, intermediate mass and mirror each weigh ≈5.6 kg. A pair of metal springs, mounted from a pre-isolated support structure, supports the two wires of the first stage. Another four springs are incorporated into the top mass, and hence support the intermediate mass.

The springs were developed from designs for Virgo [23]. They are made from Aubert & Duval Marval 18 maraging steel, chosen for its elastic limit of ≈1.6 GPa when precipitation hardened. To reduce the risk of noise from creep, the stress in the spring is kept to ⩽800 MPa. The basic shape of the spring, or *blade*, is an isosceles triangle cut from flat sheet material. The dimensions are 240 mm × 40 mm × 2 mm (length, base width and material thickness) for the top pair and 124 mm × 28 mm × 1 mm for the lower set. Rectangular areas are incorporated at the base and the tip to assist clamping: the blade is held by a clamp at its base, and a lightweight clamp holds the suspension wire near the tip. Between these clamps, the main part of the spring is pre-curved by rolling so that it lies flat and level under load.

The spring stages were designed to act as isolators with two-pole low-pass responses with characteristic frequencies of 2.7 Hz (top stage) and 3.0 Hz (intermediate stage), where uncoupled frequencies are given. For coupled frequencies and other details of the isolation performance see [22]. These stages have combined vertical transmissibility of $\sim 10^{-5}$ at 50 Hz, with the further attenuation provided by active and passive pre-isolators and the compliance of the bottom stage.

Operation of an interferometric detector requires the relative positions of the mirrors to be set and maintained to sub-wavelength precision by the overall or *global* control system. To assist this process, every suspension has a *local* control system to damp its modes. Each triple pendulum has six optical *shadow-sensors* co-located with coil-magnet actuators arrayed around the top mass. The control law employed approximates velocity feedback in the frequency range of the rigid body modes to be damped (below 10 Hz) with additional low-pass filtering to exclude noise at higher frequencies. For this damping to work efficiently, all of the modes must couple to the top stage. This can be achieved by choosing the attachment points of the connecting wires, together with other parameters such as the masses and moments of inertia of the stages, see e.g. [24]. By this means it is possible to achieve rapid settling of the suspension after a disturbance. As the actuation is at the top stage, sensor noise is strongly filtered permitting the use of devices with $\approx 10^{-10}$ m Hz$^{-1/2}$ noise. A sensing range of about 3 mm provides tolerance in the initial setup and for subsequent drift.

Due to the large 1064 nm light power in the interferometer, and finite scattering at the optical components, scattered light tends to reach every part of the internal volume of the vacuum chambers. The shadow-sensors employ silicon photodiodes and, even though they are remote from the main interferometer beams, large changes in the 1064 nm power can lead to false signals in the local controls. This causes unwanted feedback between the power in the interferometer and the positions of the mirrors. For sufficiently high power, such as the target power level planned for GEO-HF, this would lead to instability. The problem has been eliminated by adding a modulation-demodulation scheme to the local sensors to reduce their sensitivity to any light that does not carry the appropriate modulation [25]. The modulation frequency for the sensors at each suspension is chosen to minimize beats with local electrical interference (pick-up); it is typically in the range 7–10 kHz.

Global control requires faster actuation, which is therefore applied at the lower stages of the suspension. Electrostatic actuation (see below) is provided at the level of the mirror, and coil–magnet actuation is applied at the intermediate mass, where tolerable noise levels are

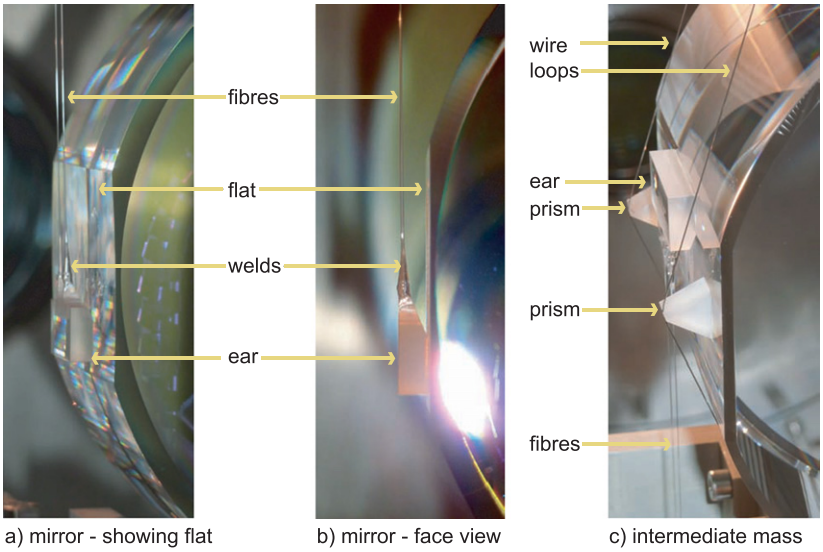

Figure 3. Three views of details of monolithic mirror suspensions as installed at GEO 600. All parts are made from fused silica. Oblique view (a) shows the ear bonded just below the centre of the flat polished on the side of the mirror. The fibres and the welds fixing them to the ear can also be seen. Panel (b) shows a face-on view of the same arrangement, while (c) is a photograph of the intermediate mass. Here the ear can be seen (above centre on the flat) and two triangular prisms are visible. These form the main interface between the wire loops from the upper stage blades and the intermediate mass—grooves in the prisms positively locate the wires.

greater. To reduce the chance of re-introducing noise, these actuators are mounted on a quiet *reaction chain* which is a triple pendulum mounted just behind the chain holding the mirror.

The triple suspension design described above has been further developed to become a four-stage (quadruple) suspension for advanced LIGO. This retains all of the essential design elements in a suspension able to carry 40 kg mirrors [26, 27]. The additional stage, together with longer blade-springs, allows improved isolation down to below 10 Hz. In the triple pendulums it had been observed that there was coupling between pitch and longitudinal actuation applied to the lower stages of the suspension. The degree of this coupling varied among different examples of the suspension, and this variation was traced to assembly tolerances that were too large. In the design of the quadruple suspension the manufacturing and assembly tolerances were reduced to ensure better consistency of the dynamical response. In other respects the GEO 600 triple suspension performed as expected. In particular there has been no evidence of excess noise or other problems due to creep in the blades or other components [28].

2.3. Monolithic suspensions

The lowest stages (i.e. the penultimate mass and the test mass itself) of the GEO 600 suspensions are formed from fused-silica masses connected by fused-silica fibres to form a quasi-monolithic suspension design with the goal of minimizing thermal noise from the suspension and test mass. Previously, long-baseline interferometers typically used metal (steel) wires to suspend the final mirror stages. However, the use of materials of lower mechanical dissipation than steel is desirable because this directly reduces the associated thermal noise. Thus,

following work which showed that fused silica could be used to fabricate low dissipation pendula of small scale [29–31], an all fused-silica design was chosen for GEO 600.

Each final mirror stage is constructed such that two fibres on each side of a penultimate mass or mirror are welded to the tips of a fused-silica attachment (or 'ear') jointed to flats on the sides of the masses by hydroxide catalysis bonding [32] (see figure 3). Thus each mirror is suspended from a penultimate mass via four fused-silica fibres.

The fused silica for the GEO 600 near and far mirrors is Hereaus Suprasil 1, and the beam-splitter material was chosen to be Suprasil 311 SV, in particular due to its low OH content and consequent low absorption at 1064 nm [33].

The fused-silica fibres (formed from Suprasil 2) are produced using a computer controlled pulling machine, where fused-silica stock material of diameter 5 mm is heated using an oxy-hydrogen flame, then pulled to form a thinner region of approximately 3 mm in diameter. This region is then heated and pulled for a second time to produce the required fibre dimensions of $\sim$220 μm diameter and 280 mm length [34].

The dimensions are chosen such that the various resonant frequencies of the modes of the final suspension stage were set to enable a pendulum mode frequency of the suspension of $\sim$1 Hz, an uncoupled vertical bounce mode frequency of $\sim$15 Hz and a first violin mode frequency of approximately $\sim$650 Hz whilst simultaneously enabling low thermal noise performance. A detailed finite element analysis model of the expected suspension thermal noise performance shows the thermal noise from the silica fibres at 50 Hz for a single suspension to be $\sim 3 \times 10^{-20}$ m Hz$^{-1/2}$ [35]. This is below the original top-level design specification of 7×10^{-20} m Hz$^{-1/2}$.

There was concern that extremely high-Q violin modes of the suspensions could couple into control loops where the actuation is applied to the lower stages of the suspensions. It was realized that it would be possible to selectively damp these modes by applying small quantities of a lossy material to short sections of the fibres. By choosing the amount of material, the violin mode frequencies could also be tuned to ensure they fell in a narrow frequency band. The material chosen had to be applied in liquid form yet be cured to a vacuum compatible state, and amorphous teflon (PTFE) was chosen [34].

The monolithic suspensions have proven reliable with over 200 fibre-years of continuous operation without failure[4], and no sign of excess noise [28]. This led to selection of similar and closely related designs for the long-baseline GWDs currently under construction.

2.4. Electrostatic drives

To achieve stable operation or to *lock the interferometer* requires a transition from a random starting point where the mirrors are moving at velocities typically of order 1 μm s^{-1} (due mainly to seismic noise), to a stable state in which the desired resonant conditions are met and maintained. In GEO 600 a key aspect of this process, locking the relative lengths of the two interferometer arms, takes $\sim$10 ms—the period during which the control signals remain valid. Maintaining lock requires feedback control of the relative lengths of the 600 m arms with a control bandwidth of $\approx$200 Hz. Together these considerations demand an actuator with suitable bandwidth and the ability to provide forces in the 0.1–1 mN range. Coil-magnet actuators were ruled out for direct mounting on the mirror due to the risk of excess noise (from magnets moving in response to stray magnetic field gradients, or as a result of the

[4] An accident during work on the interferometer led to breakage of one fibre in 2003. There have been no subsequent failures.

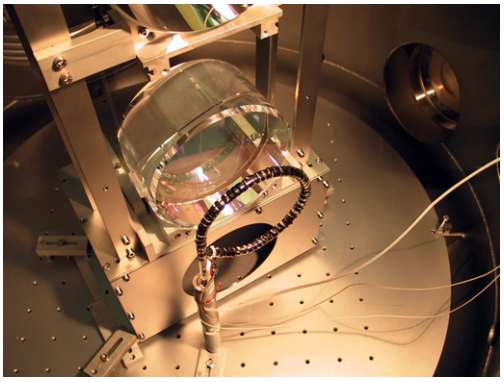

Figure 4. The GEO 600 ring heater installed behind the folding mirror MFe. For clarity, this image shows the ring heater before the installation of a reflector, and before the installation of side heaters, as mentioned in section 3.3.

mechanical properties of the magnets and the adhesive required to bond them to the mirror). Therefore, electrostatic actuation was considered.

Two simple arrangements for ESDs were rejected. The use of a parallel-plate capacitor with the mirror acting as one electrode was ruled out as it was not clear how to make the mirror conductive nor how to make a connection to it in a low-noise manner (with fused-silica suspension fibres). The option of mounting the mirror such that it jutted into the volume of a large parallel-plate capacitor was rejected, as the required voltage would exceed 10 kV, and it was not known how to generate and handle such voltages with low noise.

To reduce the required voltage to the more familiar sub-kV range, an arrangement was sought based on a finer geometry of capacitor where lower voltages would generate sufficiently strong fields. A planar electrode pattern, see figure 2, was produced by plating interleaving sets of conductive fingers of gold-on-chromium on a fused-silica mass of a size similar to an interferometer mirror. This mass constitutes the bottom stage of the reaction pendulum. The electrode pattern is placed adjacent with, parallel to and centred on the rear face of the mirror, leaving a gap of 3 mm, which is also the width of the lines and spaces of the capacitor.

To avoid unwanted damping of suspension motion the loss in the ESD circuit must be limited by ensuring that the real part of the electrical impedance is small at the sub-100 Hz frequencies of interest for suspension thermal noise. This is achieved by employing a voltage source for the ESD and keeping wiring resistance low ($\sim 10\,\Omega$). The required voltage of up to 900 V is provided by commercial TREK 601C amplifiers.

The ESD provides attractive forces proportional to the square of the applied voltage. To permit bipolar feedback, a *bias* of 630 V (i.e. half-range in terms of force) is applied. The bias also acts to linearize the response for the relatively small signals present in lock. To produce large, linear forces for lock acquisition, an electronic square-root circuit is employed before the HV amplifier. This circuit however, is too noisy for use when observing and is thus disabled following lock acquisition.

ESDs are also required for advanced LIGO and the resulting arrangement is a scaled-up version of the GEO 600 ESD for 40 kg mirrors. Finite-element methods were used to confirm, refine, and develop the design, see e.g. [36].

2.5. Ring heater

After the installation of the main mirrors in GEO 600, stable locking the power reycling cavity was not possible, the reason being a radius of curvature (RoC) mismatch of the folding mirrors at the ends of the vacuum tube. The radii of curvature were 666 m for mirror MFn and 687 m for mirror MFe, respectively (see layout in figure 1). In order to minimize the difference in radii of curvature, a ring heater element, as shown in figure 4, was placed behind mirror MFe to heat its rear surface [37]. Thermal expansion then leads to a bending of the whole mirror, reducing the RoC. By changing the heating power this radius can be adjusted. The heating element is made of a 10 mm fused-silica rod, bent into the shape of a P, with an inner diameter of 12 cm. A 100 μm thick foil of stainless steel, cut into a roughly 4 mm wide strip, is wound around the fused-silica rod. The ends of the strip are clamped to a small piece of MACOR that also clamps the power supply cables. A voltage of about 13 V resulting in a current of ca. 2.6 A is applied to the one end while the other is kept at ground potential. In this asymmetric arrangement, great care must be taken to stabilize and filter the voltage sufficiently to avoid noise coupling via electrostatic interaction with the mirror from the inhomogeneous electric field between the heater and the suspension frame and safety structure. Although this simple design was initially only meant to verify the operation principle, it worked surprisingly well and has now successfully been operating for more than a decade.

With the ring heater we can adjust the RoC of MFe sufficiently to make locking the PRC of GEO 600 possible with decent power build up. However, the ring heater allows to change the radius of curvature only in one degree of freedom. A significant fraction of the contrast imperfection of the beams from the two interferometer arms was found to result from radii of curvature mismatch in the horizontal and vertical directions. This led to the installation of additional heaters at the sides of MFe to ideally match the radii of curvature of the mirrors in the both arms horizontally, as well as vertically. The side heaters are described in section 3.3.

Recently, the ring heater has also been used to partially compensate the thermal lens in the beam splitter (BS) [25]. To do so, the ring heater power is increased with increasing laser power. To provide some extra margin for future power increases, an additional curved polished aluminum reflector has been installed behind the ring heater at the end of 2012 (not shown in figure 4). To minimize the risk of excess noise due to light scattering from the ring heater, the reflector area perpendicular to the laser beam was kept as small as possible, and the assembly was mounted on FLUOREL feet to provide some seismic isolation. The reflector increases the heating efficiency such that the power of the ring heater can be reduced 2.5 fold (to the values mentioned above) to achieve the same curvature as before the installation of the reflector. A novel method to compensate the BS thermal lens is described in section 3.2.

2.6. Signal recycling

To improve the sensitivity of an interferometer, the internal light power is increased by employing low-loss optics, keeping the output port close to a dark fringe, and adding power recycling. Gravitational waves or other oscillating arm-length changes cause light to emerge from the output in the form of modulation sidebands around the frequency of the strongly suppressed optical carrier. The sideband fields are converted to an electronic signal by mixing them with an optical local oscillator and extracting the beats that result from square-law detection within a photodiode. Before the GEO-HF upgrade, a heterodyne method was employed where the local oscillator consisted of 15 MHz RF sidebands imposed on the light entering the interferometer and transmitted to the detection optics.

SR [38] was developed to shape the frequency response of interferometers. A partially transmitting SR mirror (MSR in figure 1) is interposed between the interferometer and the photodiode to form a *SR cavity*. The properties of the signal sidebands which resonate in this cavity are determined by both the transmission and microscopic position of the SR mirror, and the reflectivity of the complex mirror formed by the interferometer. In GEO 600 the resulting response is like that of a Fabry–Perot cavity where the bandwidth is determined mainly by the transmittance of MSR, and the resonance by its microscopic position (modulo 1/2 wavelength of the light). The effective length of the cavity is the same as the unfolded length of the interferometer arms, i.e. ≈1200 m in GEO 600.

In GEO 600, SR provides the desired frequency response without requiring arm cavities. In early operation, MSR was chosen to have 2% transmission. The tuning was set at various frequencies up to 1 kHz, depending on the status of background noise during commissioning.

A significant advantage of SR is an improvement of the fringe-contrast of the whole interferometer. The curvature of the SR mirror is chosen to produce a stable optical mode in the SR cavity, or equivalently, to ensure that (most of) its higher-order spatial modes are non-resonant. This reduces the effect of optical distortions that scatter light into higher-order modes [39]. The power loss from the output of the interferometer is reduced by a factor of up to $4/T$ where T is the transmittance of the SR mirror [40]. This effect of SR, called *mode-healing* [41], is important for the operation of GEO 600 where suppression of power loss to the output and a consequent increase of the internal power have both been observed.

The addition of SR complicates operation of the interferometer as one additional length degree of freedom and two extra angular degrees of freedom must be controlled. GEO 600, without arm-cavities and therefore potentially simpler to control, has proven to be an ideal test-bed to develop control techniques for SR. With SR, the frequency response of an interferometer depends on the tuning, which may vary or drift with time. This complicates the process of calibration, and methods to cope with this have been developed, as described in the following section.

2.7. Strain calibration of GEO 600

The main science output of GEO 600, as discussed earlier in this paper, is a voltage arising from a photocurrent produced by the photodiode placed at the output of the SR cavity, or in transmission of the output mode-cleaner (see PDO in figure 1). This signal contains information about the geometric arm-length difference ΔL of the two arms of the interferometer, arising from the passing of gravitational waves of amplitude h. To estimate the equivalent GW strain h we must account for two main factors: the optical response of the interferometer in terms of output voltage per differential arm-length change, and the low-frequency suppression of the detected signal due to the control loops which keep the detector at its nominal operating point. Once we have an estimate of the differential arm-length, the strain can be calculated as $h = \frac{\Delta L}{L}$. Here L is the geometric length of each arm, which—due to the folding of the arms—is $L = 1200$ m in GEO 600.[5]

The two steps highlighted above can be practically approached by splitting the process into two phases: the first is to determine the frequency dependent response of the detector to differential arm-length fluctuations, the second is to perform an absolute calibration of the main length-control actuator, thus anchoring the measurement to a known length scale. These

[5] In addition to preparing the signal for analysis by astrophysical search teams, this calibration process provides a quantity that is independent of the state or configuration of the detector, and as such is valuable for tracking the effect of different changes and commissioning steps.

steps can be easily seen in the following calibration equation:

$$\Delta L\,[\mathrm{m}] = \frac{y\,[\mathrm{V}]}{F\,(f,\,t)\,[\mathrm{V/m}]} - x_{\mathrm{cmd}}\,[\mathrm{m}], \tag{1}$$

where y is the measured output voltage of the detector, $F\,(f,\,t)$ is the frequency and time dependent transfer function of the detector, and x_{cmd} is the differential length change resulting from the control system which keeps the detector at the desired operating point.

The control displacement, x_{cmd}, can be derived from the measured control voltages that are fed back to the electrostatic actuators. In order to do this, the actuators need to be calibrated and two different calibration methods have been developed at GEO 600. The first is to put the detector in a power-recycled Michelson configuration, mis-aligning the signal-recycling mirror, and then apply an oscillating voltage to one of the length actuators, resulting in a length change of the power-recycling cavity that can ultimately be traced back to the length of one of the input mode-cleaners; this length is typically known to an accuracy of less than 1 cm on the overall length of about 8 m. The second approach for doing this absolute calibration is to configure the detector as a simple Michelson interferometer and to, again, apply a modulated voltage to one electrostatic drive and to observe how the Michelson swings through fringes. By tracking the number of fringes as a function of the drive voltage, we can relate the voltage to the wavelength of the light, giving us a calibration in metres per volt [42].

The optical response of the detector can be estimated by applying a sequence of modulating voltages to each electrostatic drive with opposite sign, so as to induce a differential length change at the modulation frequency (see [43–45]). By then measuring the complex amplitude of these calibration signals in the detector output data stream, and by comparing them to the injected complex amplitude, the optical gain transfer function can be estimated at each of the injection frequencies. We then fit a model of the optical response to these measurements, and use this to calibrate the output data stream back to a differential measurement, as shown in equation (1). This calibration process is done in quasi-real-time, where each second of data that is recorded at the detector output is used to estimate the system parameters. Appropriate time-domain filters, which are allowed to vary slowly in time, are then used to filter the time-series data, producing a calibrated time-series of the differential length changes of the instrument.

In the current configuration of GEO 600, the optical response is well modelled by a single real pole and a gain factor. Thus, only two parameters have to be determined in order to calibrate out the detector response. In an early configuration of GEO 600, where the signal recycling cavity was detuned to a frequency around 1 kHz, and a heterodyne readout scheme was employed, the model of the optical response was more complex. This required a complex pole and a complex zero, as well as a calibration factor. Both output quadratures had to be calibrated, which then had to be combined to recover a single strain signal, containing the optimal signal level at each frequency [46]. All these methods are applicable to advanced detectors. Initial detectors other than GEO 600 have not used quasi-real-time fitting of calibration parameters.

Even though the techniques described in all the above sections were new at the time they were implemented in GEO 600, they were mature enough to incorporate them in the design of advanced LIGO and Advanced Virgo. In the following sections we will discuss techniques and upgrades of the GEO-HF project installed and tested more recently in the GEO 600 interferometer.

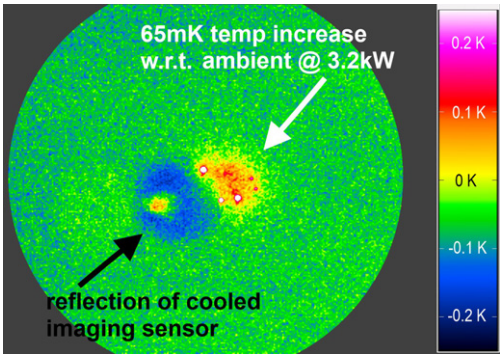

Figure 5. Thermal difference image of the partly reflecting face of the beam splitter. Clearly visible are the temperature increase due to the laser beam, a reflection of the cooled camera imaging sensor, and several small hot spots on the surface of the beam splitter.

3. Active thermal compensation

Thermal lenses and their active compensation are considered to be among the biggest challenges for advanced gravitational wave detectors.

Techniques for thermally shaping mirrors in one degree of freedom have been pioneered with a ring heater in GEO 600 (section 2.5). Virgo later used a functionally similar system [47]. We describe how the ring heater setup at GEO 600 was further extended to allow changing the mirror's shape in two degrees of freedom, by installing additional heaters.

3.1. The beam-splitter thermal lens and its measurement

The layout of GEO 600 is slightly different from advanced Virgo and aLIGO, as GEO 600 has no arm cavities. Instead, the PRC is the cavity with high finesse and large power build-up. Hence understanding and compensating the thermal lens in the BS is particularly important in GEO 600. Currently GEO 600 runs with 2–3 kW in the PRC, and the GEO-HF upgrade aims to increase the circulating power to 10–15 kW. This is challenging because the high power laser beam has to pass the BS which gets heated by the laser. The result is a thermal gradient in the BS, which will have the hottest points on the beam axis. Because the index of refraction of the BS depends on the temperature, the thermal gradient acts as a thermal lens.

The thermal lens in the BS has a negative effect on the performance of GEO 600. It changes the beam parameters for one of the interferometer arms, which results in a degradation of the interferometer contrast. As a consequence, high order modes (HOMs), which are not resonant in the PRC, leave the interferometer at the dark port. Due to this mechanism, the thermal lens lowers the power build-up in the PRC. Furthermore, the HOMs at the output of GEO 600 can couple into the TEM_{00} eigenmode of the output mode cleaner when it is not perfectly aligned or when the beam jitters. These situations result in increased shot noise and spurious signals, respectively, on the main detection PD.

Indirect measurements of the absorption of the BS have already been performed by matching optical simulations with the observed interferometer output beam [48]. Recently, we directly measured the increased temperature in the BS. A thermal imaging camera (VARIOSCAN high resolution 3021–ST) was used to measure the temperature of the BS in operation. Specifically, we made a difference measurement; we measured once in normal operation, and

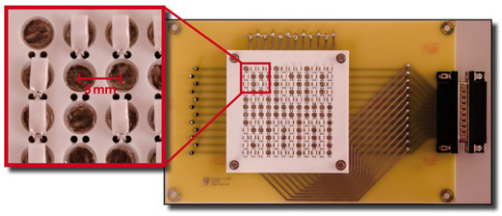

Figure 6. Photograph of a prototype heater array. Small platinum thin film resistors (white) are mounted on a ceramic plate. The ceramic plate features a small metal disk below each resistor which acts as a reflector for the infrared radiation. Not all of the resistors had been installed when the picture was taken.

once with the laser off. The resulting difference thermal image is shown in figure 5. It was found that the temperature on the BS face increases by approximately 65 mK when operating GEO 600 at 3.2 kW. We also found several small hot spots, which are most likely the result of small dust particles on the BS surface. Their influence on GEO 600 is currently under investigation. To the best of our knowledge, this is the first time a direct measurement of the *in situ* temperature of interferometer main optics has been carried out in any of the large gravitational wave observatories. It confirms the previous indirect measurements of the BS substrate absorption coefficient of 0.5 ppm cm^{-1} and can help us understand the effect of contaminations on the BS surface.

3.2. Spatially resolved heating

The thermal lens in the GEO 600 BS can be reduced by applying additional heating to the BS with a spatial profile that is inverse to the one produced by the main laser beam. In initial LIGO and Virgo, CO_2 lasers in combination with axicons have been used for an annulus heating of the arm cavity input test masses. For GEO 600 we are developing a different system for additional heating of the BS. We built a 2D matrix of 12 × 12 small heat sources, and plan to project an image of this heater matrix onto the BS surface [49]. A similar thermal actuation system is currently being developed at Virgo [50]. This setup has several potential advantages over a heating setup based on a CO_2 laser, such as laser safety, no need to stabilize a laser, and the inherent ability to project arbitrary heating patterns without changing the hardware setup. While arbitrary heating patterns would also be possible with scanning of a laser beam, this is not a viable solution for GEO 600, since the BS has full displacement sensitivity, as there are no arm cavities. CO_2 lasers, even if stabilized, could cause too much technical radiation pressure noise.

Arbitrary heating patterns may be necessary for the thermal compensation on the beam splitter of GEO 600 because the beam in the BS is oval and passes the BS at an angle. Furthermore, as the thermal image in figure 5 shows, the main laser does not only create a Gaussian heat profile. There are several very small and hot spots on the BS as well, which might be partially compensated, as far as the spacial resolution of the heater matrix will permit. The heating pattern generated by the matrix could be optimized by standard optimization schemes such as a genetic algorithm by using the power at the dark port of GEO 600 as an error signal.

Figure 6 shows a prototype 12 × 12 heater array based on thin film platinum resistors on a ceramic plate. There are small circular reflectors for each heater installed on the ceramic plate. The installation of the heater matrix is currently underway.

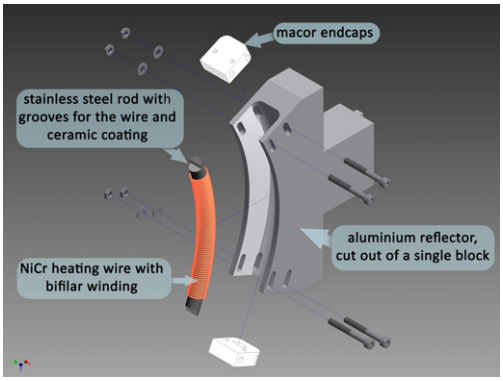

Figure 7. CAD model (exploded view) of one of the side heaters.

3.3. Side heaters

Upon studying the ring heater performance, it was found that it induced an astigmatism in the mirror RoC [51]. With the help of a finite-element model, we discovered that the non-uniform surrounding of the mirror is the cause of the astigmatism. A metal catcher close to the bottom of the mirror reflects additional radiation from the ring heater to the bottom of the mirror. Therefore, the ring heater produces a stronger mirror curvature in the vertical direction than in the horizontal direction. To counteract this astigmatism and to make an RoC adjustment possible in two degrees of freedom, we developed and installed two additional heaters at the sides of the east folding mirror (MFe in figure 1) [51] at a distance of about 10 cm from the mirror.

The design of the side heaters evolved from the ring heater and features several improvements. The main feature is an alumina coated stainless steel rod with bifilar grooves to accommodate a nichrome wire. The rod is curved, such that it is concentric to the mirror rim. A current is applied to the wire to heat it. The bifilar winding cancels the magnetic field that would be produced by the heaters. This is a measure to minimize possible coupling of noise into magnetic actuators (at the upper suspension stages), which are used to align this mirror. The whole rod functions as a heater because it is a good thermal conductor. By this means, uniform heating is still provided despite having gaps in the wiring. Figure 7 shows a CAD drawing of the side heater assembly.

Using both, the side heaters and the ring heater, we can ideally adjust the RoC of the east folding mirror in the vertical and horizontal direction independently and remove the observed astigmatism. We can change the RoC of the far east folding mirror from (horizontal/vertical) 665.5/658 ± 2 m[6] without the side heaters to 661/661 ± 2 m with the side heaters at a setting of 2.5 W. Using the side heaters, the power of HOMs at the output of the interferometer can be reduced by 37% [51]. This greatly reduces the risk of HOMs producing noise in the interferometer's gravitational wave signal, and, in combination with the ring heater, is the first realization of segmented heating (i.e. with more than one degree of freedom (DOF) being used on a GW detector.

[6] This RoC is achieved using only the ring heater.

4. The application of squeezed light

The discrete nature of photon detection causes shot-noise and limits the sensitivity of present and future gravitational wave detectors. The signal-to-shot-noise ratio can be improved by increasing the laser power, and additionally by using squeezed states of light [52, 53], as suggested by Caves in 1981 [54]. To improve the signal-to-shot-noise ratio of a differential arm length measurement, squeezed vacuum states of light need to be injected into the otherwise open output port of the interferometer, and their spatial mode overlapped with the bright light field inside the interferometer.

In the last decade considerable progress was made in realizing squeezed-light sources that fulfil the GWD requirements [55] with respect to squeezing bandwidth [56–58], squeezing strength [59–62], and compatibility of squeezed light with other gravitational wave detector techniques [63–66]. Based on these achievements, the first squeezed-light laser for continuous operation in GWDs was designed and built in 2009 [67–69], and successfully implemented in GEO 600 the following year. A non-classical noise suppression of 3.5 dB and the best sensitivity of GEO 600 up to that point was achieved [17]. This success proved the usefulness of quantum metrology and qualified the use of squeezed light as a key technology for future GW astronomy [55, 70].

Furthermore, it was shown that this achievement resembled the theoretical optimum of a quantum strategy for an interferometric measurement given the laser power used and the optical loss present in the interferometer [71]. In addition to the demonstration at GEO 600, the injection of squeezed vacuum states of light was also tested in one of the LIGO observatories [72]. While all these experiments were one-time demonstrations of squeezed vacuum applied on time scales of minutes, at GEO 600 squeezed states have now been continuously used for more than two years as described in section 4.2. This constitutes a long-term demonstration that squeezed-light injection is compatible with the tuned SR technique and DC readout. Recently investigated topics are new methods to reduce phase noise and techniques for an automatic alignment system for the squeezed beam. These are briefly reported in sections 4.3 and 4.4 below and dedicated publications are in preparation [73, 74].

4.1. The GEO 600 squeezed-light source

The compact GEO 600 squeezed-light source was set up in a class 100 cleanroom on a custom-made breadboard with the dimensions 135 × 113 cm. For the generation and control of squeezed vacuum states, three phase locked lasers are used. A fraction of the main laser at 1064 nm is frequency doubled in a second-harmonic generator, providing the required pump field at 532 nm for the nonlinear squeezing resonator (OPA). The OPA was designed as a hemilithic linear standing-wave cavity based on a plano-convex PPKTP crystal and a piezo-actuated out-coupling mirror. This single resonant cavity (finesse of 75 at 1064 nm) is length controlled by a frequency shifted and orthogonally polarized laser field (p-pol) at 1064 nm (Aux1 laser). Therefore the squeezed vacuum states (s-pol) are not contaminated at audio sideband frequencies by this control field. A second control beam, frequency shifted by 15.2 MHz (Aux2 laser), is also injected into the OPA and serves as a coherent control field for the stabilization of the 532 nm pump field phase and the 1064 nm squeezing phase. An on-board *DC* detector for local squeezing measurements proved that squeezed states of more than 10 dB over the entire bandwidth of earth-based GW detectors are generated for downstream application. A detailed description of the GEO 600 squeezer can be found in [68, 75].

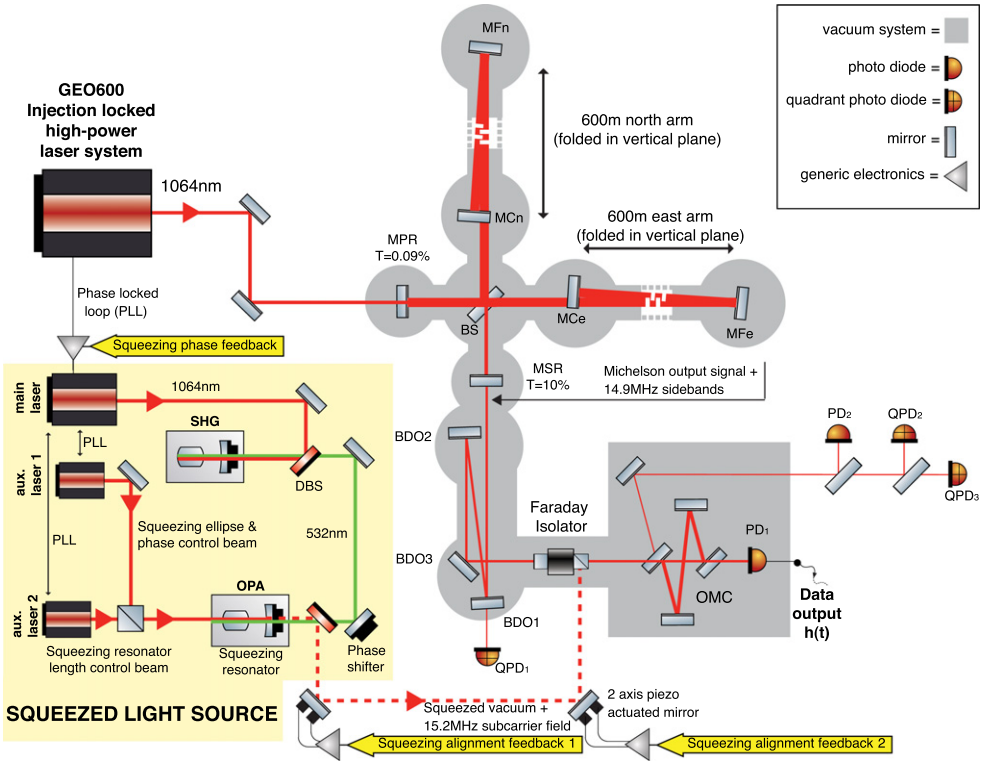

Figure 8. A simplified optical layout of the squeezed-light source (yellow box) integrated into the GEO 600 setup. For clarity some optical elements are omitted, e.g. mode-cleaner cavities and Faraday isolators. A more detailed description of the squeezed-light source and the injection path into GEO 600 can be found in [17, 68].

In May 2010, this fully assembled squeezed-light source was transported to the GEO 600 site. Figure 8 shows a simplified optical sketch of the squeezed light source integrated to the interferometer and highlights the key components discussed in the following sections.

4.2. The challenge of long-term application and results to date

Towards the goal of long-term application, the squeezed-light source of GEO 600 has been fully automated to bring its subsystems to their operating point in a reliable and orderly fashion without manual intervention [76]. Equally important is the continuous control of the squeezing quadrature angle (or *phase control*) and the squeezed beam alignment with respect to the main interferometer. By combining three new techniques, long-term application of squeezed light was demonstrated and is ongoing today [18]. The new techniques are: a novel way to generate phase control signals, automatic alignment of the squeezed beam with respect to the main interferometer, and the combination of noise locking [77] with the coherent control scheme. (See sections below for new results on these techniques.) The squeezing automation system has been extended to supervise all of these techniques as well.

Figure 9 shows histograms of observed squeezing levels at GEO 600 for two periods each about one year long. Compared to the period covering most of 2012 during which the new techniques were employed, in 2013 a general increase in the observed squeezing level

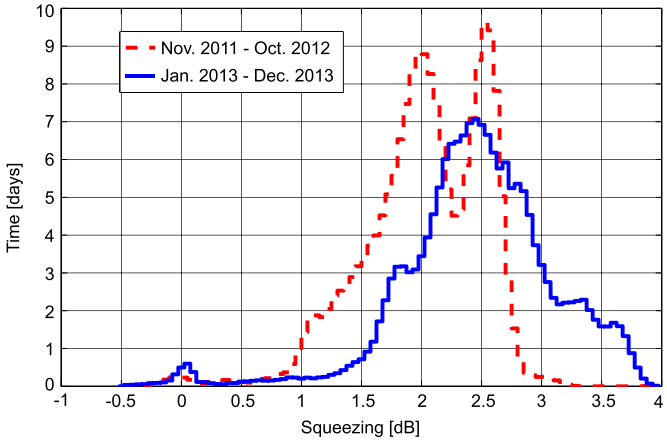

Figure 9. Histograms of the cumulative time that GEO 600 was operating in observing mode with a given squeezing level in the band from 4 to 5 kHz. In 2012, the new techniques for phase control and partial automatic alignment were introduced. In 2013, the full squeezing level of the squeezed-light source was restored (the OPA crystal had been found to be damaged after five years of operation), and optical losses were reduced. The performance for 2013 is published for the first time here.

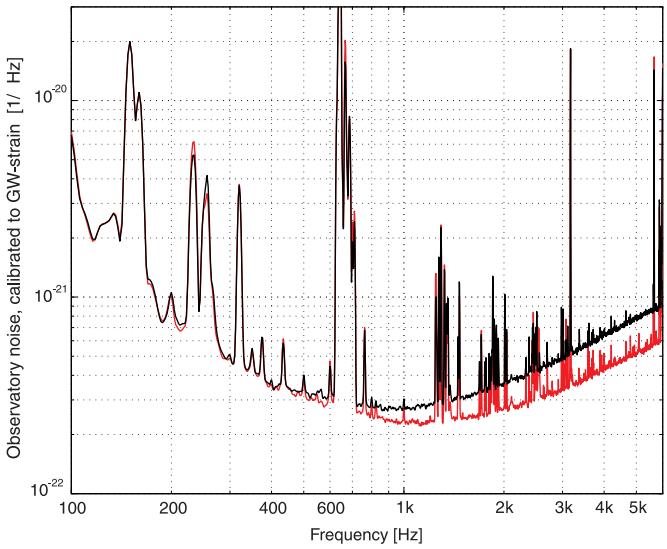

Figure 10. Strain amplitude spectral densities of GEO 600 with (red trace) and without squeezing (black trace) being applied. This measurement reflects the state of squeezing application at end of 2013. The improvement is up to 3.7 dB in the shot-noise limited frequency band. Both traces were averaged over four min. The spectral features below 700 Hz are caused by excited violin modes, calibration lines and OMC alignment control lines.

was achieved. As a result of various commissioning activities on the main interferometer as well as maintenance work on the squeezing source, the level of the obtained squeezing does

Table 1. Properties of squeezing angle error signals. Field amplitudes and powers are referenced to the total at the output port. For example, since approximately all RF sidebands are reflected by the output mode cleaner (OMC), their amplitude is 1.0 in OMC reflected. The high order modes (HOMs) for the OMC reflected case are given for the MI sidebands. In the other cases the HOMs are given for the carrier.

Port	Fields	Field amplitudes	Total power	SNR	HOMs
Pick-off before OMC	[carrier, CCSB]	[0.1, 0.1]	1/100	0.1	80%
OMC reflected	[MI sidebands, CCSB]	[1.0, 1.0]	1	1.0	< 1%
OMC transmitted	[carrier, CCSB]	[1.0, 0.1]	1/10	0.3	< 1%

vary over time. However, as an example, a stable squeezing level of 3.2 ± 0.16 dB has been achieved over the course of two weeks.

Figure 10 shows strain spectral densities of GEO 600, comparing the non-squeezed noise floor (black trace) with the squeezed noise floor (red trace) at the end of 2013. Shot-noise reduction can be observed at frequencies higher than about 400 Hz. Up to 3.7 dB of squeezing are observed in the kHz-regime. This level of squeezing is consistent with independent measurements of losses (37%) and of phase noise (20 mrad_{rms}).

4.3. Squeezing phase control

In order to achieve a constant high level of squeezing, the relative angle of the squeezing ellipse and the measurement quadrature of the interferometer needs to be continuously stabilized. Any fluctuation between these two angles is called phase noise. Some of the sources of phase noise include temperature-induced path length fluctuations, swinging suspended optics, and phase modulation from RF sidebands. New techniques to reduce phase noise have been developed at GEO 600 and are extensible to future squeezing-enhanced interferometers.

Efforts to minimize phase noise at GEO 600 are three-fold. First, steps are taken to build an intrinsically quiet squeezing source to limit the amount of fluctuations of the squeezing ellipse at its generation. This includes considerations in the mechanical design of the OPA as well as the implementation of a coherent control loop with bandwidth of 7 kHz for stabilizing the squeezing angle at the location of squeezing generation [57]. The GEO 600 OPA produces a squeezing ellipse with 9 mrad rms phase noise. Second, this stable squeezed field is in turn stabilized with respect to the local oscillator field at the point of squeezing detection using coherent control sidebands (CCSBs). Third, any slow drift of the squeezing angle or lock point errors of the phase loop are counteracted through a noise locking technique to maximize the strain sensitivity [77]. The combination of noise lock with coherent control is new, and was pivotal for long-term squeezing [18].

Recent advances on squeezing phase control at GEO 600 have focused on methods to improve the phase noise sensing at the point of squeezing detection. Historically, both at GEO 600 and at LIGO Hanford, the phase noise error signal was derived from the beat between the squeezer CCSBs [57] and the interferometer carrier light at a 1% pick-off before the output mode cleaner (OMC). This signal has both limited signal-to-noise ratio (SNR) and susceptibility to lock point errors due to higher order modes [78, 79]. A study of two alternative techniques of generating error signals at GEO 600 has demonstrated improved phase noise results. Use of interferometer RF sidebands in reflection of the OMC or

interferometer carrier light in transmission of the OMC improves the SNR and lock point errors, respectively. The photodiodes are found in figure 8 and are called QPD1, PD1, and PD2. A summary of these alternative techniques and their benefits is presented in table 1 and details are in [73].

The signal in OMC transmission has been employed for standard squeezing operation at GEO 600 since summer 2012 [18] for its reduced lock point errors and promise for future improvements in SNR. Use of this method points to specific considerations for future design of the squeezing implementation in GWDs. Reducing the CCSB frequency as low as is technically possible results in a higher transmission of these sidebands through the OMC and thus improves the SNR. This scheme also eliminates the need for an output port pick-off mirror, which otherwise increases optical losses. In addition, low noise in-vacuum RF and DC readout electronics are needed and require careful design.

Phase noise is one of the limits to quantum noise reduction that is already relevant for GEO 600 and will become even more critical as optical losses are reduced. In order to reduce rms phase noise, optical losses, and sensitivity to misalignment, the squeezing experiment at GEO 600 has developed advanced phase control techniques which contribute to achieving a higher and more stable level of squeezing. The phase control developments are pivotal towards realizing the squeezing goals of advanced detectors.

4.4. Squeezing automatic alignment

In order not to experience effective losses from misalignments, it is an important task to keep the squeezed vacuum field well aligned with the main interferometer beam and onto the OMC. Especially in the presence of suspended optics, slow alignment drifts occur that need to be compensated. Additionally, future transitions to higher observed squeezing levels will make the control of small fast alignment fluctuations more important. A significant source of such fluctuations are the 3–19 Hz dithers of the output optics as required by the currently used OMC dither alignment scheme [80].

A squeezer alignment error signal is generated using the squeezer CCSBs and the interferometer RF sidebands. The CCSBs at 15.2 MHz are resonant in the OPA and therefore share the same spatial mode as the squeezed light field and can be used as a marker. In a similar way, the 14.9 MHz RF sidebands at the interferometer output port, which have a much lower higher-order-mode content than light at the carrier frequency, are used to mark the interferometer beam's alignment. The sidebands are reflected by the OMC, and differential wavefront sensing [81] detects their beat at 300 kHz, creating error signals for the relative alignment of the squeezed light field to the interferometer beam. Two piezoelectric-actuated steering mirrors are located in the in-air part of the squeezing injection path (see figure 8) and can be used to control the alignment of the squeezed light field in all four degrees of freedom.

Active control of two alignment degrees of freedom has been routinely applied for squeezing operation since fall 2012. This is the first ever automatic alignment system for squeezed states of light. Its development at GEO 600 was first reported in [18]. Full sensing and control of all four degrees of freedom with unity-gain frequencies of 4 Hz has since been successfully demonstrated and will be adopted for continuous use in the future. A complete description of the GEO 600 squeezer automatic alignment system will be presented in [74].

5. Novel output mode cleaner alignment sensing scheme

While alignment of a cavity is a standard task in gravitational wave (GW) detection, this task becomes considerably more challenging when the cavity's input beam is dominated by

HOMs. The challenge arises because misalignments can convert some of the HOMs from the input beam into the cavity eigenmode [81–83]. This results in contamination of the error signals obtained by standard alignment techniques such as dither-locking [84]. A prime example is the alignment control of the OMCs of current and second-generation GW detectors.

A successful but ultimately limited approach to OMC alignment control is the beacon dither alignment technique [84] used by the LIGO/eLIGO [85] and GEO 600 detectors [41]. This technique applies an audio frequency modulation to the interferometer's differential arm length in order to generate a beacon that marks the mode that carries the GW signal. The scheme is completed by dithering the optics which direct the beam onto the OMC in order to find the alignment that maximizes the transmission of the beacon signal. Although this cleverly avoids coupling components of HOMs to the OMC eigenmode and can truly optimize the transmission of the GW signal, there are drawbacks. For example, HOMs introduce linear and bilinear coupling of beam jitter to the transmitted beam. Together, these couplings limit the beam directing optic dither frequencies to be well below the GW detection band and to have minimal amplitude. The consequence is a low SNR, and thus a strong limitation of the control bandwidth. In practice, even though the dither amplitudes dominate the RMS alignment fluctuations of the OMC input beam, the loops can only run with control bandwidths much lower than 100 mHz.

A new modulated differential wavefront sensing (MDWS) technique for the alignment control of a HOM-dominated beam onto a cavity has undergone preliminary testing with GEO 600's OMC. As with normal differential wavefront sensing (DWS), this technique is based on two quadrant photodiodes (QPDs) in reflection of the OMC that are separated by a relative Gouy phase of approximately 90°. The basic principle of MDWS is not unlike beacon dither alignment in that the technique aligns the GW-carrying mode to the cavity eigenmode. An important difference, however, is that MDWS does not require alignment dithers of the beam directing optics. This aspect eliminates a major source of beam jitter and can allow higher bandwidth control loops.

There are different possibilities to combine light fields for MDWS, but the variant studied here is the alignment of radio-frequency sidebands (RF SBs) at f_{RF} which are resonant in the interferometer, but are reflected by the OMC, to leakage from the OMC's internal mode modulated at f_{OMC}. In GEO 600, the OMC is used to reflect HOMs and RF SBs that are used to control the interferometer differential arm length. These SBs have low HOM content due to the low power recycling gain and large dark fringe offset they experience in the interferometer; they are therefore a good approximation of the fundamental, GW carrying mode. The OMC's length is modulated via a PZT at f_{OMC} at several kHz for its length control. Both the RF SBs as well as leakage from the OMC longitudinal modulation are found in the OMC reflected beam. Two demodulations in series, first at f_{RF} and then at f_{OMC}, result in the desired error signals.

Figure 11 presents an illustration of this scheme. We experimentally evaluated the performance of MDWS for the alignment of GEO 600's OMC using a setup similar to the one in figure 11. For this test we add the second QPD with a relative Gouy phase of 90° and send a proper linear combination of feedback to both BDO1 and BDO3 (two of the three beam directing optics which steer the laser beam onto the OMC as shown in figure 11) to be able to control all four DOFs. The resulting error points for this MDWS system have SNRs at least several times larger than those for the previously used beacon dither alignment technique. Figure 12(a) shows that the error point signals have signal content (are not sensor noise limited) all the way out to 10 Hz. To demonstrate the validity of the MDWS signals at these

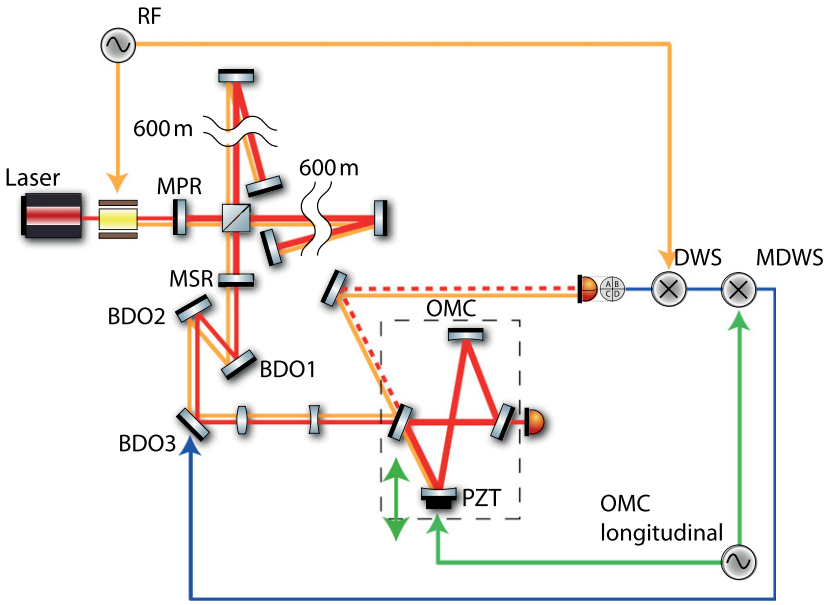

Figure 11. Simplified implementation of modulated differential wavefront sensing (MDWS) at GEO 600. Michelson RF sidebands are used as reference to be aligned onto the OMC eigenmode axis, which is marked by leakage of OMC modulation sidebands.

high frequencies, we close one of the loops with a control bandwidth of 0.1–3 Hz and observe the noise suppression with an out-of-loop sensor created by dithering BDO3 at 542 Hz. The results are displayed in figure 12. It should be noted that the BDO3 DOF is slightly rotated from the DOF which is being controlled at high bandwidth. Due to an unknown noise structure near 2 Hz in the out-of-loop sensor (figure 12(b)) which does not come from OMC alignment fluctuations in the BDO3 DOF, we cannot see the ambient noise of the controlled DOF. We therefore inject alignment dithers into BDO2 and suppress these lines using the actuation on BDO1 and BDO3 as shown in figure 12(b). The agreement between the out-of-loop and in-loop suppressions, irrespective of the slightly rotated DOFs, verifies that we are in fact controlling the OMC alignment up to 3 Hz.

To demonstrate the feasibility of this MDWS system as a replacement for the beacon dither technique of OMC alignment control, we close all four loops with DC-coupled feedback and control bandwidths below 1 Hz. For this test the beacon dither alignment system was switched off. We succeeded in obtaining stable operation of GEO 600 in this state for a period of two days. During this preliminary test we observed no more than a 5% drop in the mean optical gain of the interferometer compared to a similar time period when operating with the beacon dither alignment system.

We do not foresee any roadblocks to implementing the MDWS OMC alignment control system on a long-term basis nor to extending the control bandwidth to frequencies previously unattained. Ultimately, we expect this to replace the beacon dither alignment scheme and allow us to eliminate the dithering of the OMC input beam. In this manner we will reduce OMC RMS alignment fluctuation and lower the coupling of HOMs to the transmitted beam and ultimately to the GW channel of the interferometer.

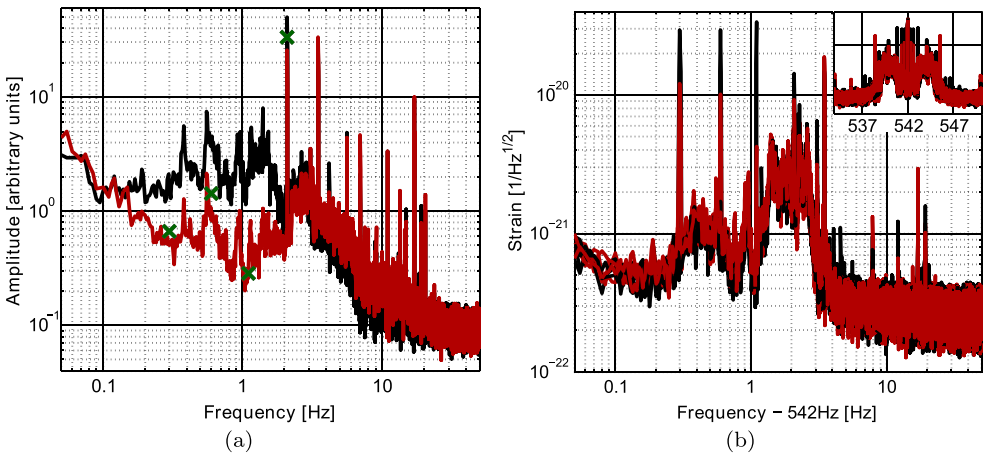

Figure 12. Demonstration of MDWS by closing an AC coupled loop with control bandwidth from 0.1–3 Hz. (a) Shows open- and closed-loop error point spectra for one of the four OMC alignment degrees of freedom (DOFs). (b) Shows an out-of-loop measure of OMC alignment fluctuations (with identical colour scheme) which demonstrates the validity of the loop used for (a). This measure is created by dithering BDO3 (figure 11) (a slightly rotated DOF from the DOF displayed in (a)) at 542 Hz and observing the sideband structure in the gravitational wave channel. The inset shows the injection line with sidebands, while the main figure shows just one side of the sideband structure expanded with a logarithmic scale. We demonstrate the effect of the loop by injecting lines separately into BDO2 (figure 11) alignment. Four injection frequencies are used (0.3, 0.6, 1.1, and 2.1 Hz) where we simply plot the spectra on top of one another. The effect of the loop can be seen by the reduction of the line heights where the reduction ratios are reflected by the green ×'s in (a) by plotting the same ratio from the open-loop (black) curve.

6. Conclusion

GEO 600 has a long history of pioneering new techniques, and in this paper we have given examples of beam tube design, triple pendulums, monolithic suspensions, ESDs, a ring heater, SR, and calibration. Second-generation detectors such as Advanced LIGO use up-scaled versions of the GEO 600 suspension design, monolithic last stage and ESDs, with the goal to increase the sensitivity of these detectors by about a factor of 10 with respect to initial LIGO. Advanced detectors such as Advanced LIGO, advanced Virgo and KAGRA all use SR (signal extraction), multi-dimensional thermal compensation systems and may use real-time calibration methods similar to the ones described here.

Today, GEO 600 continues to pioneer novel techniques, among them squeezed-light application, new thermal compensation schemes and new output mode-cleaner alignment control techniques. As one important result of this work, we highlighted that GEO 600 is the only gravitational-wave-detector that has been using squeezed light in its regular operational mode since its implementation in 2010. A new best-ever squeezing level of up to 3.7 dB is reported for the first time in this paper, as well as novel techniques for squeezing control. Demonstrating the long-term usability of squeezed states of light and how to optimally control squeezing is important input to future upgrades of advanced detectors, as well as future generation detectors in general.

Acknowledgements

The authors are grateful for support from the Science and Technology Facilities Council (STFC), the University of Glasgow, in the UK, and the Bundesministerium für Bildung und Forschung (BMBF), the Volkswagen Stiftung and the state of Lower Saxony, in Germany. This work was partly supported by the Deutsche Forschungsgemeinschaft, DFG grant SFB/Transregio 7 Gravitational Wave Astronomy. The authors further thank Stefan Goßler, Andreas Freise, Jerome Degaillaix, Josh Smith, Michal Was, Jacob Slutsky, and others for their contributions to GEO 600. We also thank Alexander Khaleidovski, Christian Gräf, and Nico Lastzka for their work on the squeezed light source. This document has been assigned LIGO document number P1400100.

References

[1] Willke B (GEO collaboration) 2002 *Class. Quantum Grav.* **19** 1377
[2] Grote H (LIGO Scientific Collaboration) 2010 *Class. Quantum Grav.* **27** 084003
[3] Abbott B P (LIGO Scientific Collaboration) 2009 *Rep. Prog. Phys.* **72** 076901
[4] Accadia T (Virgo Collaboration) 2012 *J. Instrum.* **7** P03012
[5] Takahashi R (TAMA Collaboration) 2004 *Class. Quantum Grav.* **21** S403
[6] Harry G M (LIGO Scientific Collaboration) 2010 *Class. Quantum Grav.* **27** 084006
[7] The Virgo Collaboration 2009 *Note* VIR027A09 https://tds.ego-gw.it/itf/tds/file.php?callFile=VIR-0027A-09.pdf
[8] Somiya K 2012 *Class. Quantum Grav.* **29** 124007
[9] Lück H *et al* 2010 *J. Phys.: Conf. Ser.* **228** 012012
[10] Frede M, Schulz B, Wilhelm R, Kwee P, Seifert F, Willke B and Kracht D 2007 *Opt. Express* **15** 459–65
[11] Winkelmann L *et al* 2011 *Appl. Phys.* B **102** 529–38
[12] Kwee P *et al* 2012 *Opt. Express* **20** 10617–34
[13] Heinzel G, Freise A, Grote H, Strain K and Danzmann K 2002 *Class. Quantum Grav.* **19** 1547
[14] Grote H, Freise A, Malec M, Heinzel G, Willke B, Lück H, Strain K A, Hough J and Danzmann K 2004 *Class. Quantum Grav.* **21** S473
[15] Hild S, Grote H, Hewitson M, Lück H, Smith J R, Strain K A, Willke B and Danzmann K 2007 *Class. Quantum Grav.* **24** 1513
[16] Hild S *et al* 2009 *Class. Quantum Grav.* **26** 055012
[17] Abadie J (LIGO Scientific Collaboration) 2011 *Nat. Phys.* **7** 962–5
[18] Grote H, Danzmann K, Dooley K L, Schnabel R, Slutsky J and Vahlbruch H 2013 *Phys. Rev. Lett.* **110** 181101
[19] Lück H (The GEO600-Team) 1998 The vacuum system of GEO600 *Second Edoardo Amaldi Conf. Gravitational Wave Experiments* ed E Coccia, G Veneziano and G Pizzella p 356
[20] Redhead P A 2003 *AIP Conf. Proc.* **671** 243–54
[21] Avdiaj S and Erjavec B 2012 *Materiali in Tehnologije / Mater. Technol.* **46** 161–7
[22] Plissi M V, Torrie C I, Husman M E, Robertson N A, Strain K A, Ward H, Lück H and Hough J 2000 *Rev. Sci. Instrum.* **71** 2539–45
[23] Braccini S *et al* 2000 The maraging steel blades of the Virgo super attenuator (*American Institute of Physics Conf. Series* vol 523) ed S Meshkov pp 437–8
[24] Husman M E, Torrie C I, Plissi M V, Robertson N A, Strain K A and Hough J 2000 *Rev. Sci. Instrum.* **71** 2546–51
[25] Affeldt C 2014 Laser power increase for GEO 600 *PhD Thesis* Gottfried Willhelm Leibniz University, Hannover
[26] Robertson N A *et al* 2002 *Class. Quantum Grav.* **19** 4043
[27] Aston S M *et al* 2012 *Class. Quantum Grav.* **29** 235004
[28] Sorazu B, Strain K A, Heng I S and Kumar R 2010 *Class. Quantum Grav.* **27** 155017
[29] Braginsky V B, Mitrofanov V P and Tokmakov K V 1996 *Phys. Lett.* A **218** 164–6
[30] Rowan S, Twyford S M, Hutchins R, Kovalik J, Logan J E, McLaren A C, Robertson N A and Hough J 1997 *Phys. Lett.* A **233** 303–8

[31] Cagnoli G, Gammaitoni L, Hough J, Kovalik J, McIntosh S, Punturo M and Rowan S 2000 *Phys. Rev. Lett.* **85** 2442–5
[32] Rowan S, Twyford S M, Hough J, Gwo D H and Route R 1998 *Phys. Lett.* A **246** 471–8
[33] Winkler W *et al* 2007 *Opt. Commun.* **280** 492–9
[34] Gossler S 2004 The suspension systems of the interferometric gravitational-wave detector GEO 600 *PhD Thesis* University of Hannover
[35] Kumar R 2013 Aspects of suspension design for the development of advanced gravitational wave detectors *PhD Thesis* University of Glasgow
[36] Miller J, Evans M, Barsotti L, Fritschel P, MacInnis M, Mittleman R, Shapiro B, Soto J and Torrie C 2011 *Phys. Lett.* A **375** 788–94
[37] Lück H, Freise A, Goßler S, Hild S, Kawabe K and Danzmann K 2004 *Class. Quantum Grav.* **21** 985
[38] Meers B J 1988 *Phys. Rev.* D **38** 2317–26
[39] Winkler W, Schilling R, Mizuno J, Rüdiger A, Danzmann K and Strain K A 1994 *Appl. Opt.* **33** 7547–50
[40] Meers B J and Strain K A 1991 *Phys. Rev.* D **43** 3117–30
[41] Prijatelj M 2012 Gravitational wave detection with refined light: the implementation of an output mode cleaner at GEO 600 *PhD Thesis* Leibniz Universität Hannover
[42] Leong J R *et al* 2012 *Class. Quantum Grav.* **29** 065001
[43] Hewitson M, Heinzel G, Smith J, Strain K and Ward H 2004 *Rev. Sci. Instrum.* **75** 4702–9
[44] Hewitson M *et al* 2004 *Class. Quantum Grav.* **21** 1711–22
[45] Hewitson M *et al* 2003 *Rev. Sci. Instrum.* **74** 4184–90
[46] Hewitson M *et al* 2005 *Class. Quantum Grav.* **22** 4253–61
[47] Accadia T *et al* 2013 *Class. Quantum Grav.* **30** 055017
[48] Hild S *et al* 2006 *Appl. Opt.* **45** 7269–72
[49] Wittel H 2014 Tcs matrix projection for GEO 600 https://dcc.ligo.org/LIGO-G1400525 gWADW, Takayama
[50] Day R, Vajente G, Kasprzack M and Marque J 2013 *Phys. Rev.* D **87** 082003
[51] Wittel H *et al* 2014 *Class. Quantum Grav.* **31** 065008
[52] Yuen H P 1976 *Phys. Rev.* A **13** 2226–43
[53] Walls D F 1983 *Nature* **306** 141–6
[54] Caves C M 1981 *Phys. Rev.* D **23** 1693–708
[55] Schnabel R, Mavalvala N, McClelland D E and Lam P K 2010 *Nat. Commun.* **1** 121
[56] McKenzie K, Grosse N, Bowen W P, Whitcomb S E, Gray M B, McClelland D E and Lam P K 2004 *Phys. Rev. Lett.* **93** 161105
[57] Vahlbruch H, Chelkowski S, Hage B, Franzen A, Danzmann K and Schnabel R 2006 *Phys. Rev. Lett.* **97** 011101
[58] Vahlbruch H, Chelkowski S, Danzmann K and Schnabel R 2007 *New J. Phys.* **9** 371
[59] Vahlbruch H, Mehmet M, Chelkowski S, Hage B, Franzen A, Lastzka N, Goßler S, Danzmann K and Schnabel R 2008 *Phys. Rev. Lett.* **100** 033602
[60] Polzik E S 2008 *Nature* **453** 45–46
[61] Eberle T, Steinlechner S, Bauchrowitz J, Händchen V, Vahlbruch H, Mehmet M, Müller-Ebhardt H and Schnabel R 2010 *Phys. Rev. Lett.* **104** 251102
[62] Mehmet M, Ast S, Eberle T, Steinlechner S, Vahlbruch H and Schnabel R 2011 *Opt. Express* **19** 25763–72
[63] McKenzie K, Shaddock D A, McClelland D E, Buchler B C and Lam P K 2002 *Phys. Rev. Lett.* **88** 231102
[64] Vahlbruch H, Chelkowski S, Hage B, Franzen A, Danzmann K and Schnabel R 2005 *Phys. Rev. Lett.* **95** 211102
[65] Goda K, Miyakawa O, Mikhailov E E, Saraf S, Adhikari R, McKenzie K, Ward R, Vass S, Weinstein A J and Mavalvala N 2008 *Nat. Phys.* **4** 472–6
[66] Schnabel R 2008 *Nat. Phys.* **4** 440–1
[67] Vahlbruch H 2008 Squeezed Light for Gravitational Wave Astronomy *PhD Thesis* Gottfried Wilhelm Leibniz Universität Hannover
[68] Vahlbruch H, Khalaidovski A, Lastzka N, Gräf C, Danzmann K and Schnabel R 2010 *Class. Quantum Grav.* **27** 084027
[69] Khalaidovski A, Vahlbruch H, Lastzka N, Gräf C, Danzmann K, Grote H and Schnabel R 2012 *Class. Quantum Grav.* **29** 075001

[70] McClelland D, Mavalvala N, Chen Y and Schnabel R 2011 *Laser Photonics Rev.* **5** 677–96
[71] Demkowicz-Dobrzański R, Banaszek K and Schnabel R 2013 *Phys. Rev.* A **88** 041802
[72] Aasi J (LIGO Scientific Collaboration) 2013 *Nat. Photonics* **7** 613–9
[73] Dooley K *et al* in preparation
[74] Schreiber E *et al* in preparation
[75] Khalaidovski A 2011 Beyond the quantum limit—a squeezed-light laser in GEO 600 *PhD Thesis* Gottfried Willhelm Leibniz University, Hannover
[76] Gräf C 2013 Optical design and numerical modeling of the AEI 10 m Prototype sub-SQL interferometer *PhD Thesis* Gottfried Wilhelm Leibniz Universität, Hannover
[77] McKenzie K, Mikhailov E E, Goda K, Lam P K, Grosse N, Gray M B, Mavalvala N and McClelland D E 2005 *J. Opt. B: Quantum Semiclass. Opt.* **7** 421–8
[78] Dwyer S *et al* 2013 *Opt. Express* **21** 19047–60
[79] Oelker E, Barsotti L, Dwyer S, Sigg D and Mavalvala N 2014 *Opt. Express* **22** 21106–21
[80] Prijatelj M *et al* 2010 *J. Phys.: Conf. Series* **228** 012014
[81] Morrison E, Meers B J, Robertson D I and Ward H 1994 *Appl. Opt.* **33** 5041–9
[82] Bayer-Helms F 1984 *Appl. Opt.* **23** 1369–79
[83] Anderson D Z 1984 *Appl. Opt.* **23** 2944–9
[84] Smith-Lefebvre N *et al* 2011 *Opt. Lett.* **36** 4365–7
[85] Fricke T *et al* 2012 *Class. Quantum Grav.* **29** 065005